Structure–Activity Correlations for Brønsted Acid, Lewis Acid, and Photocatalyzed Reactions of Exfoliated Crystalline Niobium Oxides

Yusuke Koito,[a] Gregory J. Rees,[b] John V. Hanna,[b] Molly M. J. Li,[a] Yung-Kang Peng,[a] Tim Puchtler,[c] Robert Taylor,[c] Tong Wang,[c] Hisayoshi Kobayashi,[d] Ivo F. Teixeira,[a] M. Abdullah Khan,[a] Hannah T. Kreissl,[a] and S. C. Edman Tsang*[a]

Exfoliated crystalline niobium oxides that contain exposed but interconnected NbO_6 octahedra with different degrees of structural distortion and defects are known to catalyze Brønsted acid (BA), Lewis acid (LA), and photocatalytic (PC) reactions efficiently but their structure–activity relationships are far from clear. Here, three exfoliated niobium oxides, namely, $HSr_2Nb_3O_{10}$, $HCa_2Nb_3O_{10}$, and HNb_3O_8, are synthesized, characterized extensively, and tested for selected BA, LA, and PC reactions. The structural origin for BA is associated mainly with acidic hydroxyl groups of edge-shared NbO_6 octahedra as proton donors; that of LA is associated with the vacant band position of Nb^{5+} to receive electron pairs from substrate; and that of PC is associated with the terminal Nb=O of NbO_6 octahedra for photon capture and charge transfer to long-lived surface adsorbed substrate complex through associated oxygen vacancies in close proximity. It is believed that an understanding of the structure–activity relationships could lead to the tailored design of NbO_x catalysts for industrially important reactions.

Introduction

Niobium oxides possess many interesting physiochemical properties, such as high-water-tolerant Brønsted and Lewis acidities, semiconducting properties, and photo- and electrochromic properties, that enable the materials to be used for a wide variety of applications such as gas sensing, catalysis, electronics, optical devices, and displays.[1–4] The structures and morphologies of niobium oxides such as HNb_3O_8, $H_4Nb_6O_{17}$, $HSr_2Nb_3O_{10}$, $HCa_2Nb_3O_{10}$, and $HTiNbO_5$ can be altered easily, which provides a structural means to achieve tunable properties for these exciting applications.[5,6] Recently, it was observed that exfoliated 2D niobium oxide structures with mostly exposed cation and anion sites exhibit a better acid and photocatalytic performance than the bulk materials.[7] However, there is a lack of understanding on their structure–activity relationships of these well-defined niobium oxides to correlate the above properties in systematic and comparative manner.

In general, solid acids are classified broadly into two types: Brønsted and Lewis acids. They exhibit different functions in acid catalytic reactions. The Brønsted acid is able to transfer protons to the substrate, whereas the Lewis acid facilitates the formation of a Lewis acid-substrate complex intermediate by the transfer of electron pairs in an electrophile–nucleophile interaction, which results in the polarization of the substrate. Consequently, Brønsted acidity can catalyze many hydrolysis and hydration reactions, whereas Lewis acidity catalyzes typical Meerwein–Ponndorf–Verley,[8] Baeyer–Villiger oxidation,[9] and glucose isomerization[10] reactions. Niobium oxides possess both Brønsted and Lewis acid properties and act as versatile catalysts to activate multistep reactions that involve both acid functions. For instance, water-tolerant, H_3PO_4-treated Nb_2O_5 can catalyze glucose transformation into 5-(hydroxymethyl)furfural under mild reaction conditions.[11] However, there is still a poor understanding of the chemical nature of Brønsted sites and the structural definition of Lewis acidity. Additionally, structural correlation with the photocatalytic properties of niobium oxides is scarcely represented in the literature. It is generally thought to relate to the electronic band structure, degree of oxygen-vacancy, and efficiency of electron–hole pair generation under light irradiation.[12] In some instances, these features and the surface acidity of niobium oxide are somehow

[a] *Dr. Y. Koito, M. M. J. Li, Y.-K. Peng, I. F. Teixeira, Dr. M. A. Khan, H. T. Kreissl, Prof. S. C. E. Tsang*
Inorganic Chemistry Laboratory
University of Oxford
South Parks Road, Oxford, Oxfordshire, OX1 3QR (UK)
E-mail: edman.tsang@univ.ox.ac.uk

[b] *Dr. G. J. Rees, Prof. J. V. Hanna*
Department of Physics
University of Warwick
Gibbet Hill Road, Coventry, CV4 7AL (UK)

[c] *Dr. T. Puchtler, Prof. R. Taylor, T. Wang*
Department of Physics, Clarendon Laboratory
University of Oxford
Oxford, OX1 3PU (UK)

[d] *H. Kobayashi*
Department of Chemistry and Materials Technology
Kyoto Institute of Technology
Matsugasaki, Sakyo-ku, Kyoto, 606-8585 (Japan)

linked to achieve desirable redox reactions, but no structural model has been given yet. A substrate-Lewis acid sites surface complex structure has been proposed to occur during the photo-oxidation reaction of benzylic alcohol on thin-layer HNb_3O_8.[13] However, no discussion has yet been given on how the photon is captured on a specific site of the niobium oxide structure and how it subsequently leads to the formation of products.

In this study, highly crystalline thin layers of related structures of exfoliated (ex) $HSr_2Nb_3O_{10}$, $exHCa_2Nb_3O_{10}$, and $exHNb_3O_8$ were synthesized carefully through an exfoliation process (as described in the Experimental Section) from the respective bulk materials. These exfoliated sheets maintain the 2D crystal structures to form precisely defined atomic structures. This can facilitate the examination of the origins of solid Brønsted and Lewis acidity and more importantly photocatalysis related to these acidities in a comparative manner based on atomic scale and quantum chemical levels, which is not well understood for most poorly defined solid acid materials. Thus, their structural integrities, degrees of distortion of the octahedra and defects, acidities, and band structures of these thin-layer structures were characterized extensively by using XRD, multinuclear solid-state NMR spectroscopy, EPR spectroscopy, X-ray photoelectron spectroscopy (XPS), cyclic voltammetry (CV), UV/Vis spectroscopy, and time-resolved photoluminescence spectroscopy (TRPL) and compared. Model reactions, which include the hydrolysis of ethyl acetate (Brønsted acid catalyzed reaction), the conversion of pyruvic aldehyde to lactic acid (Lewis acid catalyzed reaction), the air oxidation of benzyl alcohol to benzaldehyde, and hydrogen production from water (photocatalysis), with niobium oxides have been examined. The structural aspects of the unique photocatalytic properties of these high-surface-area, 2 D, layered niobium oxide structures are discussed in particular.

Results and Discussion

The bulk Nb^{IV}-containing structures, $HSr_2Nb_3O_{10}$, $HCa_2Nb_3O_{10}$, and HNb_3O_8, are presented in Figure 1 a. The first two belong to the class of layered perovskite structures, $AB_2Nb_3O_{10}$, that contain 12 corner-shared NbO_6 units with Sr^{2+} or Ca^{2+} at the B sites. These compounds consist of negatively charged perovskite sheets that stack to form a 2D layered structure interleaved with H^+ in the A sites to compensate for the negative charge of the sheets. The Sr^{2+} ion (ionic radius of 1.58 a in 12 coordination) at the B site fits very well into the layered perovskite structure (Figure 1 i a and b). However, the occupancy of smaller Ca^{2+} cations (ionic radius of 1.48 a with a higher charge density reduces the dimensions of the perovskite layer, decreases the symmetry (Figure 1 i i a and b), and causes a substantia distortion to the individual NbO_6 units than that of larger Sr^{2+} ions.[14] However, apart from corner-sharing NbO_6 HNb_3O_8, the structure also contains edge-sharing NbO_6,[15] and H^+ cations are placed between the 2D anion sheets. The XRD patterns of bulk and exfoliated $HSr_2Nb_3O_{10}$, $HCa_2Nb_3O_{10}$, and HNb_3O_8 samples were collected (Figure 2 a). Notably, the intensities of the (0 0 4) and (0 0 6) peaks caused by layer stacking

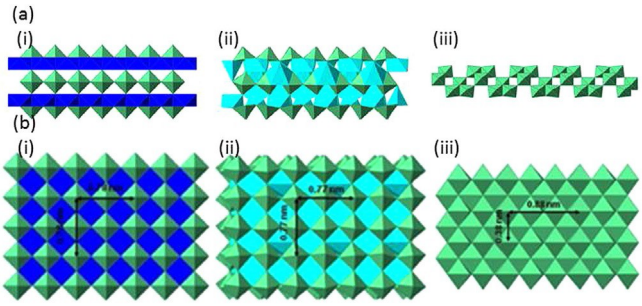

Figure 1. a, b) Two views of the crystal structures i) $HSr_2Nb_3O_{10}$, ii) $HCa_2Nb_3O_{10}$, and iii) HNb_3O_8 according to the ISCD database. GaussView5.0 was used to reproduce the structures. Atoms are labeled as follows: Nb (green), Sr (dark blue), and Ca (light blue).

along the z axis for $exHSr_2Nb_3O_{10}$ and $exHCa_2Nb_3O_{10}$ decrease significantly after exfoliation, although much broader and weaker (0 0 2) diffraction peaks are still observed even after the exfoliation process. This indicates that there was no long-range layer stacking of the materials, and thin exfoliated layers are produced. The TEM images of the exfoliated samples shown in Figure 2b indeed depict the thin nanosheet morphology, in which a flakelike 2D nanosheet structure that ranges from one to eight layers is evident for the samples.

Proton sites on shared NbO_6 units and Brønsted acidity

The solid-state ^1H magic-angle spinning (MAS) NMR (ssNMR) spectra shown in Figure 3 a, c, and e reflect the different chemical environments of protons in $HSr_2Nb_3O_{10}$, $HCa_2Nb_3O_{10}$, and HNb_3O_8. The protons are resident between the three bulk negatively charged crystalline niobium layer oxides of the strongest Brønsted acidity (BA) and they resonate in the range of $d = 9.8–11.2$ ppm. A clear shift to lower frequencies along with a decreased and broadened peak intensity is observed in the exfoliated materials because of the collapse of the layer structures as discussed previously by Takagaki et al.[16] As a result, analysis of ^1H SSNMR spectra can reflect the new chemical environment of surface-attached protons with different degrees of connectivity of the NbO_6 octahedra over these different forms of exfoliated niobium oxides. For the surface-exposed sheets, the ^1H chemical shift indicates acidity, and hydrogen species with a high downfield shift are expected to possess stronger Brønsted acidity. Clearly, the layered structure of $exHSr_2Nb_3O_{10}$ contains stacked NbO_6 octahedra in the highest symmetry with primarily shared corners that give the lowest average proton chemical shift value (the distribution curve with the most probable peak at $d_{iso} = 4.6$ ppm is shown in Figure 3 b) with the weakest BA (Figure 3 b). Comparatively, the structurally distorted octahedra in the case $exHCa_2Nb_3O_{10}$ can lead to sites with a stronger BA (assigned to the peak at $d_{iso} = 6.3$ ppm; Figure 3 d). Conversely the layered structure of HNb_3O_8 contains stacked NbO_6 octahedra with shared edges, which gives the comparatively strong BA ($d_{iso} = 7.0$, 6.5, and 5.9 ppm; Figure 3 f). Notably, the strongly acidic BA site on Group IV–VI oxides is associated with exposed bridging hydroxyl groups between octahedra with shared edges or faces,

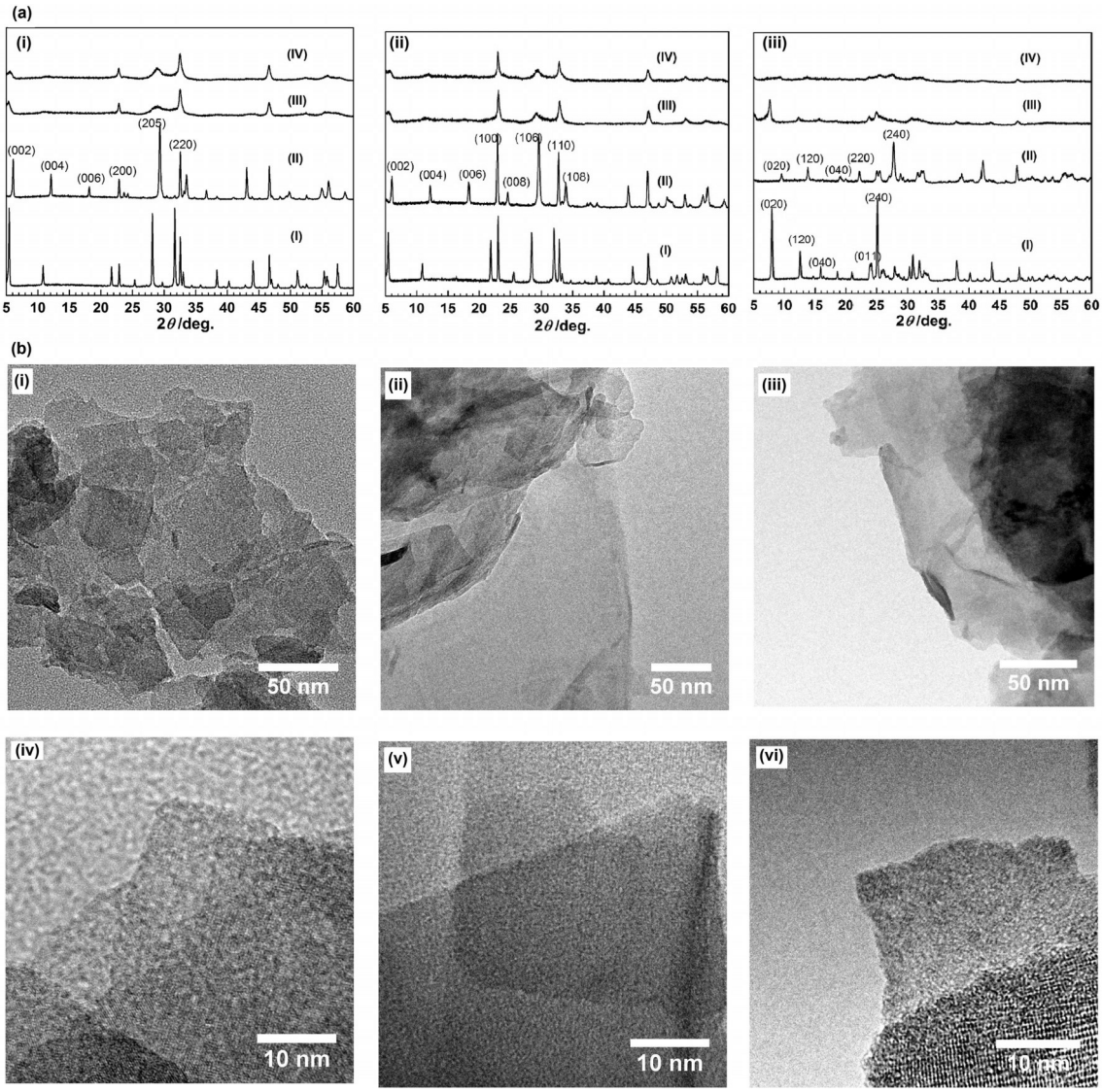

Figure 2. a) XRD patterns of i) $HSr_2Nb_3O_{10}$, ii) $HCa_2Nb_3O_{10}$, and iii) HNb_3O_8: I) hydrated crystal precursor, II) formed from I by calcination at 150 8C for 3 h, III) synthesized by exfoliation from II and IV formed from III by calcination at 150 8C for 3 h. b) TEM and HRTEM images of i, ii) $exHSr_2Nb_3O_{10}$, iii, iv) $exHCa_2Nb_3O_{10}$, and v and vi) $exHNb_3O_8$.

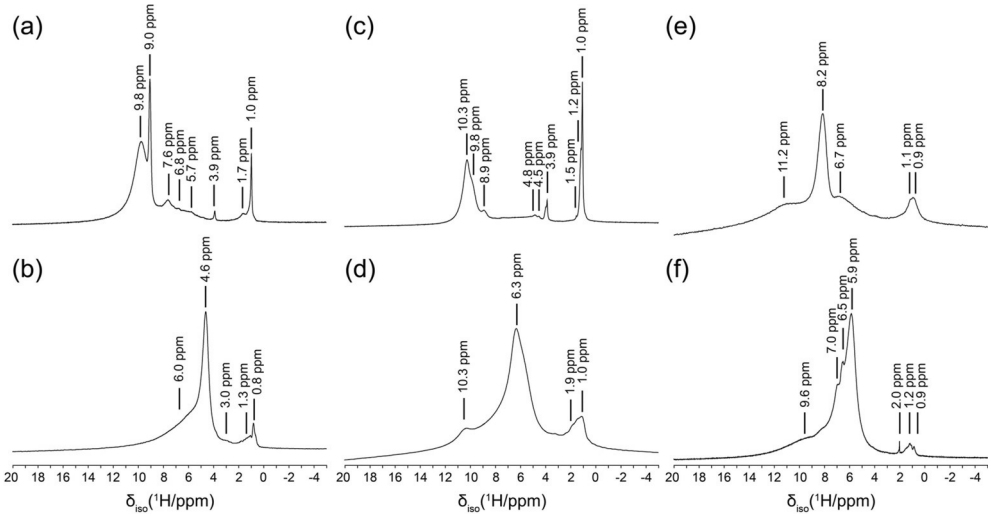

Figure 3. ^1H MAS (30 kHz) NMR spectra at 14.1 T of a) $HSr_2Nb_3O_{10}$, b) $exHSr_2Nb_3O_{10}$, c) $HCa_2Nb_3O_{10}$, d) $exHCa_2Nb_3O_{10}$, e) HNb_3O_8, and f) $exHNb_3O_8$. The isotropic shift (d_{iso}) is given above each resonance.

whereas the weaker BA corresponds to a proton localized on a terminal oxygen atom.[16] We realized that the relationship between the ^{1}H chemical shift of the ssNMR spectra and acid strength is complex so quantitative analysis cannot be performed easily.[16] The conventional NH_3 temperature-programmed desorption (TPD) technique was attempted, however, the strong adsorption and the facile nature of the single layers induced a significant degree of structural collapse so no clear desorption profiles could be obtained for the quantitative analysis. Nevertheless, according to the BET analysis (Figure S1), $exHSr_2Nb_3O_{10}$, $exHCa_2Nb_3O_{10}$, and $exHNb_3O_8$ have surface areas of 53, 56, and 112 $m^2 g^{@1}$, respectively. Thus, the quantity and strength of the Brønsted acidity is in the order: $exHNb_3O_8$ > $exHCa_2Nb_3O_{10}$ > $exHSr_2Nb_3O_{10}$. The activity for the BA-catalyzed hydrolysis of ethyl acetate[16] also gives the same order. The measured rates for ethanol production from ethyl acetate over $exHSr_2Nb_3O_{10}$, $exHCa_2Nb_3O_{10}$, and $exHNb_3O_8$ are 0.10, 0.12, and 0.20 *m*mol min$^{@1}$, respectively (Figure 4).

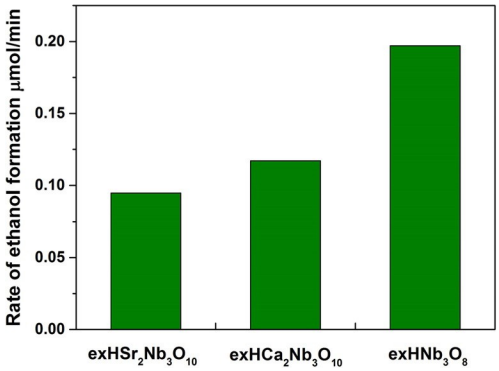

Figure 4. Catalytic performance in the hydrolysis of ethyl acetate. A mixture of 1.9 mL ethyl acetate, 0.1 mL water, and 50 mg catalyst was heated in a vacuum vial with a fluoro-rubber cap at 333 K for 20 h.

Distorted NbO_6 units and Lewis acidity

In general, the position of the LUMO of Lewis acid (LA) sites (cationic sites) are responsible for the formation of a stable LA-nucleophilic reactant adduct that, consequently, enhances LA catalytic reactions.[17] The LUMO energy can correspond to the conduction band edge in the solid catalyst, which implies that Lewis acids with a lower energy of the conduction band edge (E_{CB}) are advantageous to activate Lewis acid catalyzed reactions.

UV/Vis spectra of layered and exfoliated $HSr_2Nb_3O_{10}$, $HCa_2Nb_3O_{10}$, and HNb_3O_8 and the corresponding Kubelka–Munk plots against the energy of light are presented in Figure 5. The estimated band gap energies of $exHSr_2Nb_3O_{10}$, $exHCa_2Nb_3O_{10}$, and $exHNb_3O_8$ are 3.30, 3.39, and 3.29 eV, respectively.[18] Furthermore, we used E_{CB} & 1.23@Eg/2[19] to estimate the lowest conduction band potential of each niobium oxide as @0.42, @0.47, and @0.42 eV for $exHSr_2Nb_3O_{10}$, $exHCa_2Nb_3O_{10}$, and $exHNb_3O_8$, respectively. These results show that $exHCa_2Nb_3O_{10}$ has a more negative CB edge potential, which presumably reflects the degree of structural distortion

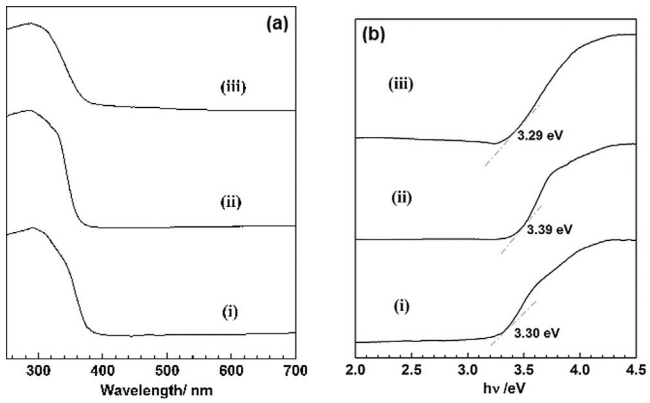

Figure 5. a) UV/Vis absorption spectra of i) $exHSr_2Nb_3O_{10}$, ii) $exHCa_2Nb_3O_{10}$, and iii) $exHNb_3O_8$; b) Transformed Kubelka–Muck plot versus the energy of light of i) $exHSr_2Nb_3O_{10}$, ii) $exHCa_2Nb_3O_{10}$, and iii) $exHNb_3O_8$.

of the NbO_6 units caused by the polarization of Ca^{2+} in the B site. This observation matches our extended X-ray absorption fine structure (EXAFS) data (Table S1), which show a significant distortion of the NbO_6 units to longer Nb@O bonds (2.51 a) if they face the high-charge-density Ca^{2+} in the B site in $exHCa_2Nb_3O_{10}$ (to maintain charge neutrality, shorter Nb@O bonds of 1.66 a are created simultaneously). The degrees of distortion in both $exHSr_2Nb_3O_{10}$ and $exHNb_3O_8$ are similar and minor. Blasse et al. reported the relationship between the crystal structures and energy delocalization of perovskite structures that consist of corner-sharing NbO_6 octahedral units.[20] According to their study, the relatively stronger interaction between the NbO_6 octahedra with B cations results in the localization of the excited state energy because the bond angle of Nb@O@Nb is far from the ideal angle of 1808, that is, the NbO_6 octahedral units are tilted. Clearly, the localization of the excited state energy causes the position of the absorption band edge to be shifted to a shorter wavelength with a weaker Lewis acidity.

The chemical nature of Nb species was further investigated by using XPS (Figure 6 a). The main signals of Nb $3d_{5/2}$ and Nb $3d_{3/2}$ of $exHSr_2Nb_3O_{10}$ and $exHNb_3O_8$ appear at a slightly higher binding energy (BE) than that of $exHCa_2Nb_3O_{10}$. In the case of $exHSr_2Nb_3O_{10}$ and $exHNb_3O_8$, the BE of Nb $3d_{3/2}$ was at 210.35 and 210.43 eV, respectively. However, for $exHCa_2Nb_3O_{10}$, this peak was observed at BE = 209.52 eV indicative of the more distorted and reduced nature of $exHCa_2Nb_3O_{10}$. Therefore, the conduction band level of Nb^{5+} in $exHCa_2Nb_3O_{10}$ is apparently higher than that of the other two exfoliated niobium oxide samples because of the polarization distortion of NbO_6 by Ca^{2+}. We used CV to probe the reduction potential of Nb^{5+} sites in $exHCa_2Nb_3O_{10}$. The reduction potential of $exHNb_3O_8$ was @0.82 V (vs. AgCl), which is slightly higher than that of @0.86 V of $exHSr_2Nb_3O_{10}$ (Figure 6 b). However, $exHCa_2Nb_3O_{10}$ shows that a significantly low potential of @1.10 V is required to reduce the Nb^{5+} site in $exHCa_2Nb_3O_{10}$. As a result, from the correlation of the conduction band energy level with the Lewis acidity of the three exfoliated samples, the order of Lewis acidity is expected to be $exHNb_3O_8$ + $exHSr_2Nb_3O_{10}$ @ ex-

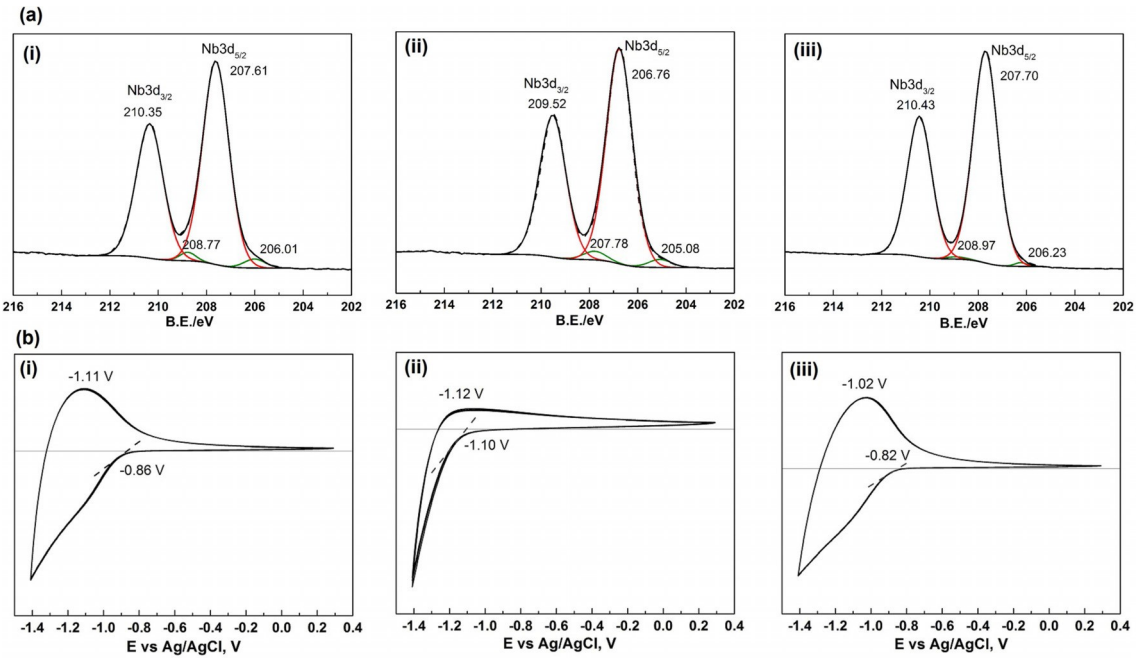

Figure 6. a) XPS spectra of i) $exHSr_2Nb_3O_{10}$, ii) $exHCa_2Nb_3O_{10}$, and iii) $exHNb_3O_8$. The spectra fitting was conducted by using Casa XPS. b) Cyclic voltammograms of $exHSr_2Nb_3O_8$, $exHCa_2Nb_3O_{10}$, and c) $exHNb_3O_8$.

$HCa_2Nb_3O_{10}$. This result is in good agreement with the results obtained by using UV/Vis spectroscopy, EXAFS, and XPS.

It is accepted that Lewis acids can promote the conversion of pyruvic aldehyde to lactic acid.[17] Their catalytic performance (yield and rate) depends on the LUMO energy position in homogeneous Lewis acid site or the lowest conduction band position in solid Lewis acids.[17] Thus, this reaction can be used as a chemical probe to illustrate the effectiveness of the exfoliated niobium oxide samples. The conversion of pyruvic aldehyde and the yield of lactic acid over $exHSr_2Nb_3O_{10}$, $exHCa_2Nb_3O_{10}$, and $exHNb_3O_8$ are shown in Figure 7. Despite the small difference in the catalytic activity of $exHSr_2Nb_3O_{10}$ and $exHNb_3O_8$, they consistently exhibit a higher yield of lactic acid than $exHCa_2Nb_3O_{10}$ per gram or mole of sample per unit time. The apparent low catalytic performance of $exHCa_2Nb_3O_{10}$ can be attributed to the higher conduction band energy caused by structural distortion, which weakens the binding of pyruvic aldehyde to lead to lactic acid. Thus, the polarization distortion of NbO_6 by the B site cation appears to play an important role to determine the Lewis acidity of the layered niobium oxide structures.

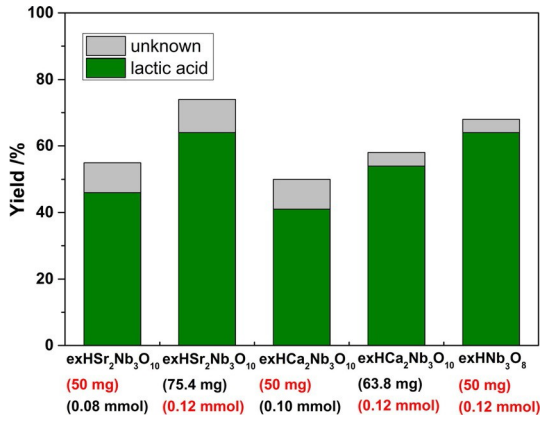

Figure 7. Catalytic yield of lactic acid from after 2 h reaction over three exfoliated samples. A mixture of catalyst (50 mg) and aqueous pyruvic aldehyde solution (0.1 m, 2.0 mL) was heated in a vacuum vial with a fluoro-rubber cap at 383 K. Comparison can be made with a normalized quantity of catalysts (in mg or in mmol marked in red).

Distorted NbO_6, Nb=O, lattice vacancies, and photocatalysis

Photocatalysis is a complex phenomenon, and there is very little knowledge about how the structures of exfoliated niobium oxides correlate to their photoactivity. However, it is believed that the samples must contain "chromophore" groups that can capture appropriate photonic energy and transfer it to a substrate-solid complex to catalyze chemical reactions on a longer timescale. Thus, the elucidation of the chemical nature of the chromophore groups and the sites for the substrate-solid complex is crucially important to understand their structure–activity relationships in photocatalysis. Notably, the lifetime of this substrate-solid complex for energy transfer in a redox manner in photocatalysis should be long enough to initiate typical chemical reactions ($10^{@10}$–$10^{@5}$ s).[21] Therefore, the formation of stable substrate-niobium oxide complexes through a Lewis acid–base interaction would be preferable for effective electron migration under UV irradiation. In addition, the contribution of oxygen-vacancy sites cannot be underestimated as the trapping of a substrate onto an oxygen-vacancy site favors binding stabilization.

First, EPR spectroscopy was used to demonstrate the formation of oxygen-vacancy sites in these exfoliated samples. The spectrum of $exHNb_3O_8$ shows a clear signal at $g = 2.01$ (Figure 8 a), which is assigned to a free unpaired electron trapped on an oxygen-vacancy site (O_v).[22] Only a very weak or marginal signal is observed in the EPR spectra of $exHCa_2Nb_3O_{10}$ and $exHSr_2Nb_3O_{10}$. Therefore, O_v sites were produced with highest density in the $exHNb_3O_8$ structure. Interestingly, another small signal at $g = 1.98$ is noted in the spectrum of $exHCa_2Nb_3O_{10}$, which could be assigned to the Nb^{4+}. Generally, Nb^{4+} species have a very short spin relaxation time.[23] This signal could only be confirmed at & 4 K.[24]

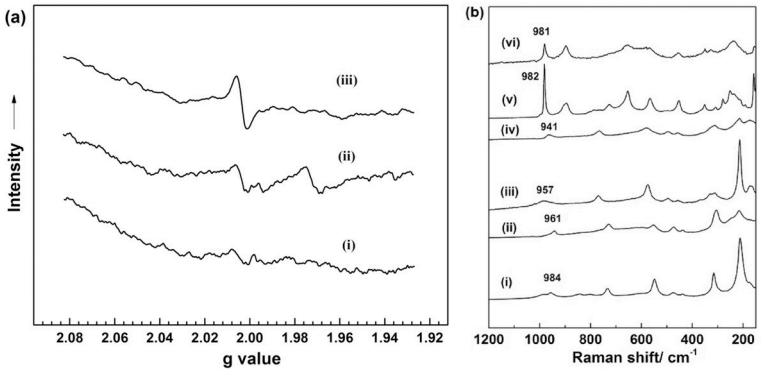

Figure 8. a) EPR spectra of i) $exHSr_2Nb_3O_{10}$, ii) $exHCa_2Nb_3O_{10}$, and iii) $exHNb_3O_8$ measured at ambient temperature. b) Raman scattering spectra of i) $HSr_2Nb_3O_{10}$, ii) $exHSr_2Nb_3O_{10}$, iii) $HCa_2Nb_3O_{10}$, iv) $exHCa_2Nb_3O_{10}$, v) HNb_3O_8, and vi) $exHNb_3O_8$.

The Raman spectra of bulk crystalline and exfoliated $HSr_2Nb_3O_{10}$, $HCa_2Nb_3O_{10}$, and HNb_3O_8 are shown in Figure 8 b. Interestingly, the energetic lattice vibration was observed at $\tilde{n} = 950–990\ cm^{@1}$, which can be assigned to the terminal Nb=O bond.[25] Thus, the signal at $\tilde{n} = 961\ cm^{@1}$ observed in the spectrum of $exHCa_2Nb_3O_{10}$ is apparently higher in wavenumber than that of $exHSr_2Nb_3O_{10}$ ($\tilde{n} = 941\ cm^{@1}$), presumably because of the polarization distortion of NbO_6 by the small Ca^{2+} (B site) in the layer perovskite structure, as discussed. However, it is interesting that both bulk HNb_3O_8 and $exHNb_3O_8$ give the most intense and sharp signal at $\tilde{n} = 981\ cm^{@1}$, which clearly suggests a high content of Nb=O. It is not yet known why the HNb_3O_8 structure can give rise to a high degree of Nb=O (reflected by using Raman spectroscopy) and O_v (reflected by using EPR spectroscopy) defects. Presumably, their formation may relate to the electronic and structural effects caused by the edge-sharing octahedra. Such a simultaneous formation of terminal Nb=O and O_v of NbO_6 in the HNb_3O_8 structure could maintain the oxidation state of Nb (+5).

Static photoluminescence (PL) and time-resolved photoluminescence (TRPL) spectroscopy were conducted to reveal the fundamental photoelectron excitation and energy transfer processes in the time domain. The PL spectra of $exHNb_3O_8$, $exHSr_2Nb_3O_{10}$, and $exHCa_2Nb_3O_{10}$ are shown in Figure 9 a. Clearly, $exHNb_3O_8$, which had the highest content of Nb=O terminal bonds, gave the most intense PL signal at **1** = 400–700 nm followed by $exHCa_2Nb_3O_{10}$ and then $exHSr_2Nb_3O_{10}$ upon excitation at 266 nm. Thus, it is evident that Nb=O can act as a chromophore to take up this photon energy, which can then be transferred to radiative processes from **1** = 400–700 nm through lattice relaxation. TRPL decay curves recorded during the UV irradiation are shown in Figure 9 b, and the decay constants and amplitudes of each decay component are summarized in Table 1. There is a fast decay component of the radiative recombination of the excited electrons and holes because of the relaxation of the excited Nb=O structure. The relaxation time of the excited Nb=O bond in $exHNb_3O_8$, $exHCa_2Nb_3O_{10}$, and $exHSr_2Nb_3O_{10}$ is inversely related to their Raman vibration frequency (Nb=O bond strength): 165 ps, $\tilde{n} = 981\ cm^{@1}$; 343 ps, $\tilde{n} = 961\ cm^{@1}$; and 552 ps, $\tilde{n} = 941\ cm^{@1}$, respectively. However, there is also a slow decay observed, which is ascribed to the recombination of excited electrons and holes of Nb@O. The decay constant of the fast component is 165 ps for $exHNb_3O_8$, which is substantially faster than that of $exHSr_2Nb_3O_{10}$ (552 ps) and $exHCa_2Nb_3O_{10}$ (343 ps). In addition, in the case of $exHNb_3O_8$, the amplitude of the decay is more than sevenfold higher than that of $exHSr_2Nb_3O_8$ and $exHCa_2Nb_3O_{10}$, which reflects that $exHNb_3O_8$ has the largest amount of Nb=O chromophore. In contrast, the slow components (t & 1.5–2.0 ns) show no pronounced difference in terms of lifetime and amplitude for all the three exfoliated samples. It is thought that the coexistence of O_v in close proximity in $exHNb_3O_8$ may offer a recombination centre or intermediate pathway for the rapid relaxation of excited Nb=O after the capture of the photon energy (Scheme 1).

Table 1. Experimental TRPL parameters of $exHNb_3O_8$, $exHSr_2Nb_3O_{10}$, and $exHCa_2Nb_3O_{10}$.

Catalyst	Fast component		Slow component	
	Decay constant [ps]	Amplitude	Decay constant [ps]	Amplitude
$exHSr_2Nb_3O_{10}$	552	1312	2033	1654
$exHCa_2Nb_3O_{10}$	343	1382	1796	2098
$exHNb_3O_8$	165	9861	1532	3408

Interestingly, there is no significant change of the Raman Nb=O peak of $exHNb_3O_8$ at $\tilde{n} = 981\ cm^{@1}$ in comparison to that of the bulk crystalline sample ($\tilde{n} = 982\ cm^{@1}$), although $exHSr_2Nb_3O_{10}$ and $exHCa_2Nb_3O_{10}$ show clear redshifts of 16 and 23 $cm^{@1}$, respectively, after exfoliation (Figure 8 b). The ^{93}Nb NMR spectra shown in Figure 10 provide similar structural information to the Raman spectra. The exfoliation of the samples causes a decrease in the local symmetry, which gives a corresponding broadening in the ^{93}Nb NMR spectra. The chemical shift of ^{93}Nb depends on the oxygen coordination of the Nb site.[26] The large positive shift observed (& 300 ppm) after the exfoliation of the $HSr_2Nb_3O_{10}$ and $HCa_2Nb_3O_{10}$ complexes is attributed to the relaxation of NbO_6 units during the exfoliation process. In contrast, the $exHNb_3O_8$ spectra show no clear shift.

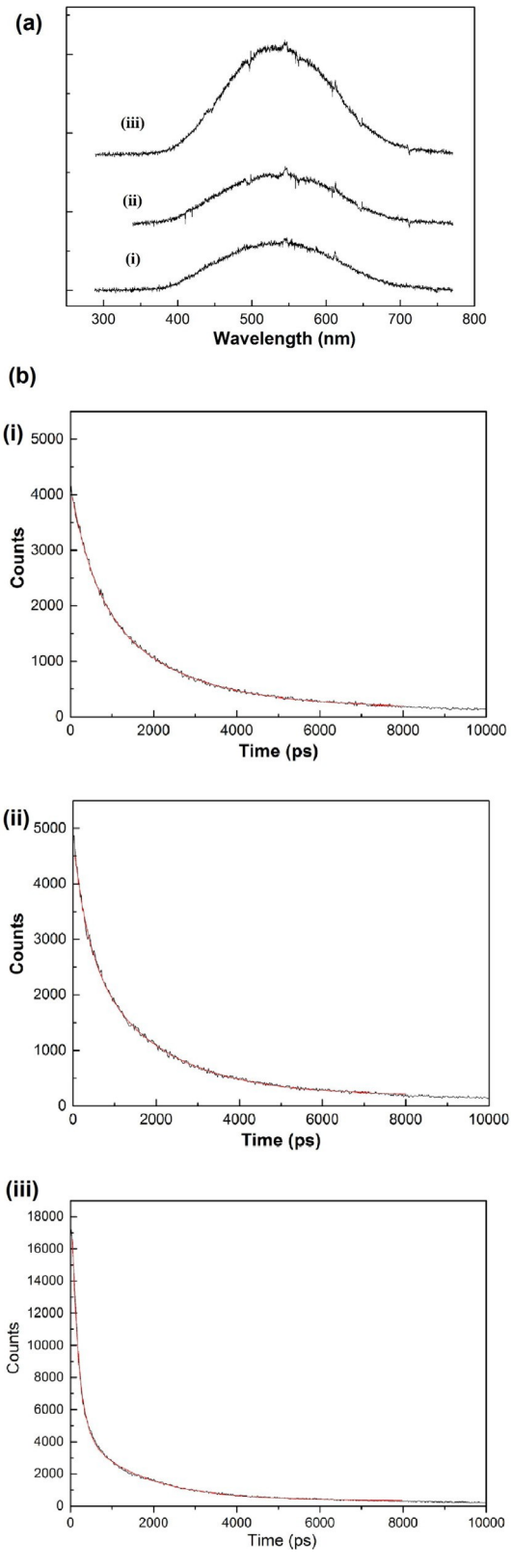

Figure 9. a) PL spectra of i) $exHSr_2Nb_3O_{10}$, ii) $exHCa_2Nb_3O_{10}$, and iii) $exHNb_3O_8$ and b) TRPL spectra of i) $exHSr_2Nb_3O_{10}$, ii) $exHCa_2Nb_3O_{10}$, and iii) $exHNb_3O_8$. The decay curve is fitted by a red line according to the equation:

$$y = y_0 + A_1 \exp\left(\frac{-(x - x_0)}{t_1}\right) + A_2 \exp\left(\frac{-(x - x_0)}{t_2}\right)$$

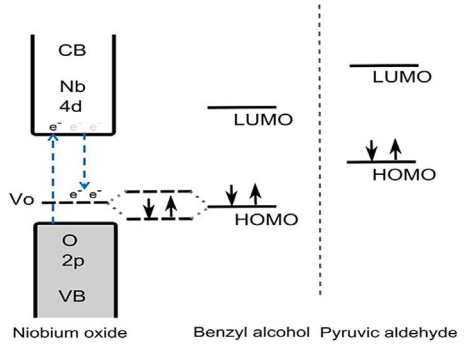

Scheme 1. Schematic of an energy diagram that depicts the CB edge (mainly contributed to by the vacant 4d band of Nb), VB edge (mainly contributed to by the filled O2p band) and oxygen vacancies with electron transfer under UV irradiation and their relationship with the HOMO levels of benzyl alcohol and pyruvic aldehyde.

This implies that the formation of Nb=O terminal bonds stabilizes the Ni site and prevents structural relaxation. The broadening of the spectra after exfoliation for $exHSr_2Nb_3O_{10}$ and $exHCa_2Nb_3O_{10}$ mean they can no longer be deconvoluted reliably to the substituted crystal sites (Table 2). This is expected as the symmetry has been reduced dramatically by the distortion of the NbO_6 units. Conversely, despite the broadening of $exHNb_3O_8$, the resonance can still be deconvoluted into two

Table 2. Experimentally measured ^{93}Nb NMR isotropic shift (d_{iso}) data for the crystal and exfoliated samples. To determine the d_{iso}, the line broadening and shift parameters were allowed to iterate in the Topspin SOLA function, and all other NMR interactions were kept constant. "na" denotes that no d_{iso} could be measured.

Niobate	Site	d_{iso} [ppm]	
		Crystal	Exfoliated
$HSr_2Nb_3O_{10}$	A	@981	na
	B	@996	na
	C	@1013	@794
$HCa_2Nb_3O_8$	A	@1053	na
	B	@1055	@763
HNb_3O_8	A	@1072	@1063
	B	@1046	@1050

Nb sites : this is expected as the formation of Nb=O terminal bonds would maintain some of the local symmetry. The EPR spectra presented in Figure 8a show an appreciable increase in the amount of oxygen vacancies for $exHNb_3O_8$. If we compare the lack of shift in the corresponding ssNMR and Raman spectra, it can be presumed that the oxygen vacancies also alleviate the distortion of the NbO_6 units. Many physiochemical properties of niobium oxides are derived from their structural distortion and the presence of defect sites. The exposure of [NbO] sites by exfoliation is useful to enhance these properties provided that the structure is still maintained. Notably, the structure rigidity of the HNb_3O_8 structure is clearly retained after the exfoliation process.

The catalytic performance for the photo-oxidation of benzyl alcohol to benzaldehyde[12] as a test reaction for the three exfoliated samples is shown in Figure 11a. The $exHNb_3O_8$ sample

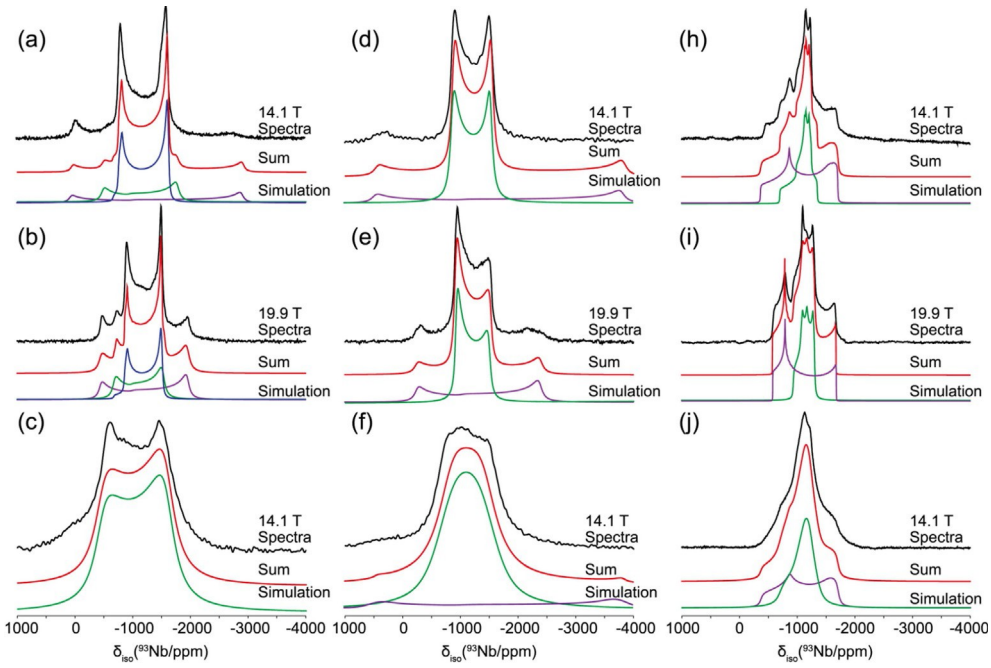

Figure 10. ^{93}Nb static NMR spectra of $HSr_2Nb_3O_{10}$ crystals at a) 14.1 and b) 19.9 T, c) $exHSr_2Nb_3O_{10}$, $HCa_2Nb_3O_{10}$ crystals at d) 14.1 and e) 19.9 T, f) $exHCa_2Nb_3O_{10}$, HNb_3O_8 crystals at g) 14.1 and h) 19.9 T, and i) $exHNb_3O_8$. The simulation of the individual deconvoluted resonances is shown below each spectrum, and their sum is given in red.

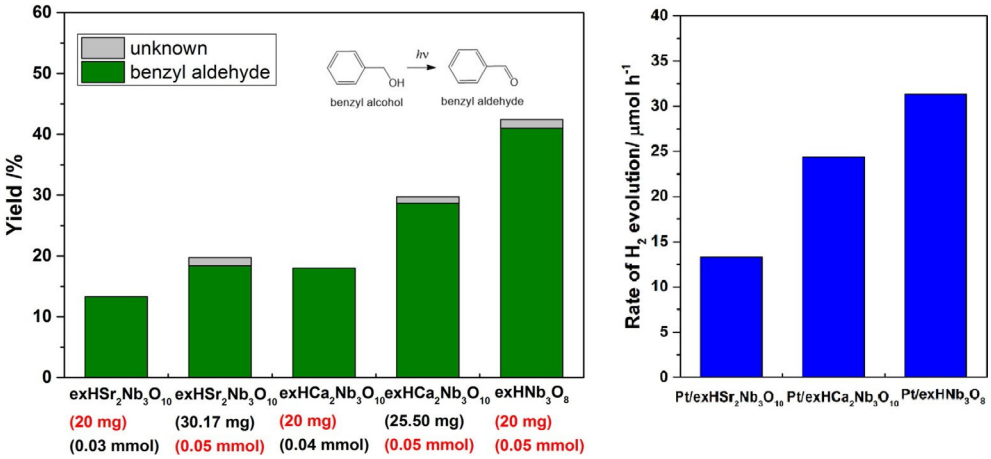

Figure 11. a) Catalytic yields of the photo-oxidation of benzyl alcohol into benzaldehyde after 20 h. A mixture of benzyl alcohol (0.0258 mL) and powder catalyst (20 mg) was added to BTF (7.5 mL) and stirred under UV irradiation at ambient temperature. A comparison can be made with the normalized quantity of catalysts (in mg or in mmol, marked in red). b) Photocatalytic hydrogen evolution over various catalysts. A mixture of water (90 mL), methanol (10 mL), and catalyst (20 mg) was agitated under UV irradiation for 2 h at room temperature.

gives 41% yield of aldehyde from the photo-oxidation of benzyl alcohol, which is significantly higher than that of $exHSr_2Nb_3O_{10}$ (18%) and $exHCa_2Nb_3O_{10}$ (29%) with the same amount of catalyst used (0.05 mmol). It is generally thought that substrate adsorption takes place mainly on a Lewis acid site in a photocatalyst.[12] However, Lewis acid catalyzed reactions can be fundamentally different from photocatalysis. Interestingly, it is apparent that the order of Lewis acidity of the three exfoliated samples ($exHNb_3O_8$ + $exHSr_2Nb_3O_{10}$ @ $exHCa_2Nb_3O_{10}$) is not consistent with the order of catalytic performance in this photo-oxidation reaction.

Similarly, photocatalytic hydrogen evolution over Pt-loaded exfoliated samples was evaluated under UV excitation using a sacrificial reagent (methanol).[27] No H_2 production was observed over the exfoliated samples without Pt. The H_2 evolution rates in the presence of the three exfoliated samples upon irradiation are displayed in Figure 11b. The order of the rates H_2 evolution of the Pt-loaded samples is $exHNb_3O_8$ > $exHCa_2Nb_3O_{10}$ > $exHSr_2Nb_3O_{10}$, which also corroborates well with that of photocatalytic oxidation of benzyl alcohol. Clearly, the photocatalysis of the two reactions reflects the order of the relative contents of Nb=O and O_v. It is believed that Nb=O as

a chromophore is responsible for the capture of the photon and that O_v can trap the oxygenated substrate.

If we consider the reaction scheme from an energy perspective, it is argued that the introduction of O_v in $exHNb_3O_8$ can compete with the direct affinity of Lewis acidic Nb^{5+} for the substrate to form a more stable substrate-catalyst complex. Particularly, the conjugated carbonyl group from benzaldehyde is expected to give a lower HOMO position than the reactive pyruvic aldehyde (Scheme 1). The high HOMO energy of pyruvic aldehyde is relatively favorable to interact with the CB edge of the Nb Lewis acid site directly but only at the excited state, whereas benzaldehyde is anticipated to interact relatively more easily with the oxygen-vacancy site at a compatible energy level for the effective binding of this substrate for sufficient time to induce photocatalysis.

We summarize a proposed mechanism for the superior photocatalytic activity for benzyl alcohol oxidation over $exHNb_3O_8$ layers in Scheme 2. First, the oxygen vacant site binds the hydroxyl group in benzyl alcohol strongly. This allows the chromophore group (Nb=O) in close proximity to transfer its photon energy for chemical conversion. The UV photon energy captured by Nb=O produces excited electrons on the Nb^{5+} Lewis acid site to interact with adsorbed benzyl alcohol species through conjugated phenolic ring and prolongs charge separation in this stable LA-complex (photocatalytic reduction). During this prolonged period of time, electron-deficient terminal and bridging oxygen atoms can abstract hydrogen atoms from the adsorbed benzyl alcohol (Scheme 2 iv). The activation of O_2 from the air by the regenerated oxygen vacant site after the desorption of benzaldehyde can also lead to the take up of hydrogen atoms to form H_2O_2 as a side product (photocatalytic oxidation).[12] For hydrogen evolution from water splitting, it is thought that the capture of photons by Nb=O in $exHNb_3O_8$ allows the excited electrons to migrate to the Pt surface (2 nm Pt particle; Figure S2) at the materials interface for the catalytic reduction of H^+ on the appropriate timescale,[27] whereas the hole (positively charged terminal oxygen atom) will oxidize the adsorbed methanol at the prolonged relaxation time.

Conclusions

Exfoliated crystalline niobium oxides that contain exposed but interconnected NbO_6 octahedra with different degrees of structural distortion and defects have been demonstrated to catalyze Brønsted acid, Lewis acid, and photocatalytic reactions efficiently. It is shown that the catalytic performances of these reactions are highly dependent on the structural connectivity of the NbO_6 octahedra, their distortions, and their defects. The structure–activity relationships are presented. We believe that this study could lead to the understanding and rational optimization of niobium oxide structures for more efficient catalysis in these reactions.

Experimental Section

Materials and synthesis

Nb_3O_8, $KSr_2Nb_3O_{10}$, and $KCa_2Nb_3O_{10}$ as chemical precursors were first synthesized by conventional solid-state syntheses from their physical mixtures using stoichiometric amounts of K_2CO_3, Nb_2O_5, Sr_2CO_3, and Ca_2CO_3.[28–30] The protonated forms were then produced by agitation of these obtained powders in excess 4 m HCl solution repeatedly over 24 h. The preparation of exfoliated samples was conducted by using an intercalator reagent, *tetra*-butyl ammonium hydroxide (TBAOH) solution. The host crystals of HNb_3O_8, $HSr_2Nb_3O_{10}$, and $HCa_2Nb_3O_{10}$ that possess layer structures were held by acidic protons within their crystallographic planes. If they were soaked in aqueous TBAOH solution (pH > 11.0), amine molecules were inserted into each layer to result in layer segregation by weakening the interlayer stacking.[5, 6] After centrifuging at 3000 rpm for 5 min, the supernatant solution was mixed with 1 m HNO_3 to give a white precipitate immediately. The obtained precipitate was then washed with distilled water until the pH of the filtered solution became neutral and the sample was then dried at 80 8C. For the synthesis of the Pt nanoparticles, a mixture of hexachloroplatinic acid ($H_2PtCl_6 \cdot 6\,H_2O$; 62.1 mg), polyvinylpolypyrrolidone (PVP; M_w = 45000; 133 mg), and ethanol (180 mL) were heated to reflux for 3 h. The solvent was evaporated, and the residue was dispersed into water/ethanol ($V_{water}/V_{ethanol}$ = 1:1, 50 mL).[31] The Pt-loaded catalysts were prepared by sonicating the mixture of niobium oxide and Pt colloidal solution for 3 h. The dispersed

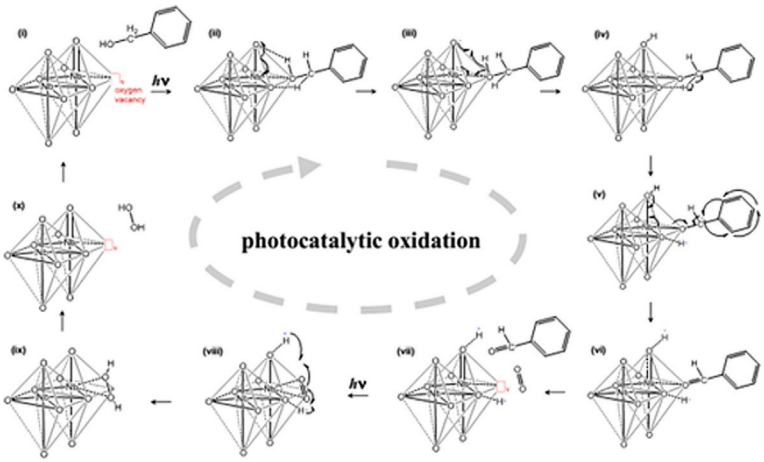

Scheme 2. Proposed reaction mechanism of benzyl alcohol oxidation over exfoliated niobium oxides under UV irradiation.

solution was centrifuged at 5000 rpm for 5 min and the obtained precipitate was washed with water and ethanol. Finally, the filtered samples were dried naturally at RT for a few days. To remove the PVP residue, the obtained samples were placed under UV irradiation, which led to the photodecomposition of the PVP layer that encapsulated the nanoparticles.[32]

Catalytic reactions

The hydrolysis of ethyl acetate into ethanol was performed in a sealed Pyrex tube that contained a mixture of ethyl acetate (1.9 mL), water (0.1 mL), and catalyst (0.12 mmol). After 20 h at 333 K, ethanol product was extracted by adding water (5 mL) into the product solution, followed by analysis by using HPLC. The catalytic activities of exfoliated niobium oxides were examined for the conversion of pyruvic aldehyde to lactic acid in water. This reaction involved heating a mixture of catalyst (0.05 g) and aqueous pyruvic aldehyde (0.1 m, 2.0 mL) in a sealed Pyrex tube at 383 K for 2 h. The product solution was analyzed by using HPLC. For the photocatalytic oxidation of benzyl alcohol to benzaldehyde, a mixture of benzyl alcohol (0.0270 g), catalyst (20 mg), and benzotrifluoride (BTF; 7.5 mL) were stirred in a tightly closed flask (25 mL) under UV irradiation for 20 h after the solution was presaturated with O_2. The resultant solution was then analyzed by using ^{1}H NMR spectroscopy (Bruker Avance III HD nanobay 400 MHz NMR).

For the hydrogen evolution experiments, the reaction was conducted with dispersed catalysts (20 mg) in a mixture of methanol (10 mL) and distilled water (90 mL). Before the reaction, that the solution was bubbled with 5% CH_4/Ar, of which CH_4 was used as an internal reference. This mixture was agitated under UV irradiation for 2 h, and the obtained gas was analyzed by using GC (Agilent 7890A) fitted with a flame ionization detector (FID).

NMR spectroscopy

All solid-state ^{93}Nb NMR spectra were recorded at 14.1 T (n_0= 146.71 MHz) and 19.9 T (n_0=208.10 MHz) by using Bruker Avance II+ and Avance III spectrometers, respectively. A Bruker static 5 mm broadband probe was used at each field. The spectra were referenced to the primary standard; saturated K[$NbCl_6$] in dry acetonitrile (d_{iso} = 0 ppm).[33] A solid echo (p/4–t–p/4) pulse sequence that employed a 250 kHz nonselective pulse was utilized with a relaxation time of 500 ms, and a minimum of 4096 transients were collected for each experiment. The resonances with a width of over 250 kHz were collected by using a variable offset cumulative frequency stepped (VOCS) method.[34, 35] Spectral simulation was completed using the Topspin SOLA function. To fit the exfoliated samples, the isotropic shift (d_{iso}) and broadening parameters were allowed to iterate, and the CSA and quadrupolar determined interactions were fixed to the bulk crystal parameters determined previously (Table S2). If it was not viable to distinguish the resonance (because of the dramatic broadening caused by exfoliation), the fit was removed from the deconvolution.

The ssNMR data were collected at 14.1 T (n_0=599.44 MHz) by using a Bruker Avance II+ spectrometer. A 30 kHz MAS frequency was applied by using a Bruker 2.5 mm double air-bearing HX probe. The spectra were referenced to the secondary standard alanine, which gives three resonances at d_{iso}=1.1 (CH_3), 3.5 (CH), and 8.5 ppm (COOH) with respect to TMS (d_{iso}=0 ppm).

TRPL spectroscopy

The sample was excited by using a frequency-tripled Ti:Sapphire laser (266 nm) that gave & 150 fs pulses with a repetition frequency of & 7.57 MHz. This beam was passed through a reflecting x36 objective lens (0.5 NA) onto the sample. The emitted signal was passed back through the same lens to an Andor Shamrock 303i spectrometer by using an iDus 420 charge-coupled device (CCD). For TRPL spectroscopy, the beam was directed to an output slit in the spectrometer (with a window of & 10 nm) and passed to a photomultiplier tube (PMT) detector (Becker and Hickl PMH-100, with an instrument response function (IRF) & 200 ps) connected to a PicoQuant TimeHarp 260 TCSPC card (resolution 25 ps).

XPS

XPS spectra were recorded by using a Thermo Scientific K-Alfa XPS instrument equipped with a microfocused monochromated Al X-ray source. The source was operated at 12 keV, and a 400 micron spot size was used. The analyzer operated at the analyzer energy (CAE) of 200 eV for survey scans and 50 eV for detailed scans. Charge neutralization was applied using a combined low-energy/ion-flood source. The data acquisition and analysis were conducted by using CasaXPS (Casa software Ltd.). The peak position was referenced to the C 1s peak of the carbon tape at BE = 285.00 eV,[36] and peak fitting was applied by using a Lorentzian/Gaussian (L/G) 30 % curve.

UV/Vis spectroscopy, XRD, BET surface area analysis, Raman spectroscopy, CV, EPR spectroscopy, and TEM

The crystalline phase of the samples was identified by using powder XRD (X' pert Pro, PANalytical, operated in Bragg–Brentano focusing geometry and using CuK_a radiation (l = 1.5418 a) from a generator operated at 40 kV and 40 mA). TEM images of the samples were recorded by using JEOL 2010 electron microscope with a high-resolution pole piece. The UV/Vis adsorption spectra were recorded by using a UV/Vis spectrometer (Lambda 750S, PerkinElmer) with KBr as the reference.

The specific surface area was derived from the corresponding adsorption isotherms with a conventional BET nitrogen adsorption apparatus (micromeritics 3flex). The samples were dried at 150 8C under vacuum for 24 h before the experiments.

Raman spectra were measured by using a Raman Microscope (Renishaw) with a laser excitation wavelength of 532 nm. An exposure time of 10 s, and eight scans were adopted for each experiment. These samples were dried at 150 8C before the measurements.

For CV measurements (Ivium, CompactStat), the scan was recorded by measuring the potential across the membrane that hosted the catalysts on the tip of an electrode, which was prepared by drying a mixture of the catalyst (10 mg), Nafion (Nafion D-521 dispersion, 5% w/w in water and 1-propanol, > 0.92 meq $g^{@1}$ exchange capacity, 10 *m*L), and milliQ water (1 mL) to stabilize the membrane. The electrolyte used was 0.1 m aqueous KCl solution. A sweeping voltage in the range of 0.3 to @1.4 V at 50 mV $s^{@1}$ was used.

Acknowledgements

We are grateful to the EPSRC for supporting the work at the University of Oxford. Y.K. would like to acknowledge postdoctoral

funding from the Uehara Memorial Foundation Research Fellow- ship to enable him to work at Oxford. J.V.H. thanks the University of Warwi the EPSRC, and the Birmingham Science City for access to the 14.1 T solid state MAS NMR instrumentation used in this research. The lat was funding obtained through the Bir- mingham Science City Advanced Materials Project 1: Creating and Characterising Next generati Advanced Materials project, with support from Advantage West Midlands (AWM) and the Eu- ropean Regional Development Fund (ERDF). addition, J.V.H. ac- knowledges the UK 850 MHz Solid State NMR National Facility also used in this research which was funded by the EPSR BBSRC (contract reference PR140003), and the University of Warwick, which included partial funding through Birmingham Science C Advanced Materials Projects 1 and 2 supported by Advantage West Midlands (AWM) and the European Regional Development Fund (ERDI Collaborative assistance from the UK 850 MHz Facility Manager (Dinu Iuga, University of Warwick) is also acknowledged.

[1] Y. Zhao, C. Eley, J. Hu, J. S. Foord, L. Ye, H. He, S. C. Tsang, *Angew. Chem. Int. Ed.* 2012, *51*, 3846–3849; *Angew. Chem.* 2012, *124*, 3912–3915.
[2] B. Varghese, S. C. Haur, C. T. Lim, *J. Phys. Chem. C* 2008, *112*, 10008– 10012.
[3] D. D. Yao, R. A. Rani, A. P. O'Mullane, K. Kalantar-zadeh, J. Z. Ou, *J. Phys. Chem. C* 2014, *118*, 476–481.
[4] R. A. Rani, A. S. Zoolfakar, J. Z. Ou, M. R. Field, M. Austin, K. Kalantar- zadeh, *Sens. Actuators B* 2013, *176*, 149–156.
[5] A. Dias, S. Lima, D. Carriazo, V. Rives, M. Pillinger, A. Valente, *J. Catal.* 2006, *244*, 230–237.
[6] C. Tagusagawa, A. Takagaki, S. Hayashi, K. Domen, *J. Phys. Chem. C* 2009, *113*, 7831–7837.
[7] a) Q. Wu, Y. Yan, Q. Zhang, J. Lu, Z. Yang, Y. Zhang, Y. Tang, *ChemSu- sChem* 2013, *6*, 820–825; b) Z.-J. Yang, Y.-F. Li, Q.-B. Wu, N. Ren, Y.-H. Zhang, Z.-P. Liu, Y. Tang, *J. Catal.* 2011, *280*, 247–254.
[8] A. Corma, M. E. Domine, S. J. Valencia, *J. Catal.* 2003, *215*, 294–304.
[9] M. Renz, T. Blasco, A. Corma, V. Forn8s, R. Jensen, L. Nemeth, *Chem. Eur. J.* 2002, *8*, 4708–4717.
[10] Y. Rom#n-Leshkov, M. Moliner, J. A. Labinger, M. E. Davis, *Angew. Chem. Int. Ed.* 2010, *49*, 8954–8957; *Angew. Chem.* 2010, *122*, 9138–9141.
[11] K. Nakajima, Y. Baba, R. Noma, M. Kitano, J. N. Kondo, S. Hayashi, M. Hara, *J. Am. Chem. Soc.* 2011, *133*, 4224–4227.
[12] G. Niu, X. Guo, L. Wang, *J. Mater. Chem. A* 2015, *3*, 8970–8980.

13] S. Liang, L. Wen, S. Lin, J. Bi, P. Feng, X. Fu, L. Wu, *Angew. Chem. Int. Ed.* 2014, *53*, 2951–2955; *Angew. Chem.* 2014, *126*, 2995–2999.
14] K. Maeda, T. E. Mallouk, *J. Mater. Chem.* 2009, *19*, 4813.
15] K. Akatsuka, G. Takanashi, Y. Ebina, N. Sakai, M.-a. Haga, T. Sasaki, *J. Phys. Chem. Solids* 2008, *69*, 1288–1291.
16] a) A. Takagaki, M. Sugisawa, D. Lu, N. J. Kondo, M. Hara, K. Domen, S. Hayashi, *J. Am. Chem. Soc.* 2003, *125*, 5479–5485; b) A. Takagaki, D. Lu, N. J. Kondo, M. Hara, S. Hayashi, K. Domen, *Chem. Mater.* 2005, *17*, 2487–2489.
17] Y. Koito, K. Nakajima, H. Kobayashi, R. Hasegawa, M. Kitano, M. Hara, *Chem. Eur. J.* 2014, *20*, 8068–8075.
18] R. Ljpez, R. Gjmez, *J. Sol-Gel Sci. Technol.* 2012, *61*, 1–7.
19] Y. Matsumoto, *J. Solid State Chem.* 1996, *126*, 227–234.
20] a) M. Wiegel, M. H. J. Emond, E. R. Stobbe, G. J. Blasse, *Phys. J. Phys. Chem. Solids* 1994, *55*, 773–778; b) G. Blasse, L. G. J. de Haart, *Mater. Chem. Phys.* 1986, *14*, 481–484.
21] A. L. Linsebigler, G. Lu, J. T. Yates, Jr., *Chem. Rev.* 1995, *95*, 735.
22] F. Liao, Y. Huang, J. Ge, W. Zheng, K. Tedsree, P. Collier, X. Hong, S. C. Tsang, *Angew. Chem. Int. Ed.* 2011, *50*, 2162–2165; *Angew. Chem.* 2011, *123*, 2210–2213.
23] A. Folli, J. Z. Bloh, A. Lecaplain, R. Walker, D. E. Macphee, *Phys. Chem. Chem. Phys.* 2015, *17*, 4849–4853.
24] J. Kiwi, J. T. Suss, S. Szapiro, *Chem. Phys. Lett.* 1984, *106*, 135–138.
25] L. J. Burcham, J. Datka, I. E. Wachs, *J. Phys. Chem. B* 1999, *103*, 6015– 6024.
26] J. V. Hanna, K. J. Pike, T. Charpentier, T. F. Kemp, M. E. Smith, B. E. Lucier, R. W. Schurko, L. S. Cahill, *Chem. Eur. J.* 2010, *16*, 3222–3239.
27] J. Xiong, L. Wen, F. Jiang, Y. Liu, S. Liang, L. Wu, *J. Mater. Chem. A* 2015, *3*, 20627–20632.
28] T. Ban, S. Yoshikawa, Y. Ohya, *J. Colloid Interface Sci.* 2011, *364*, 85–91.
29] Y.-S. Han, I. Park, J.-H. Choy, *J. Mater. Chem.* 2001, *11*, 1277–1282.
30] K. Saruwatari, H. Sato, T. Idei, J. Kameda, A. Yamagushi, A. Takagaki, K. Domen, *J. Phys. Chem. B* 2005, *109*, 12410–12416.
31] R. M. Rioux, H. Song, J. D. Hoefelmeyer, P. Yang, G. A. Somorjai, *J. Phys. Chem. B* 2005, *109*, 2192–2202.
32] L. R. Baker, G. Kennedy, M. Van Spronsen, A. Hervier, X. Cai, S. Chen, L. W. Wang, G. A. Somorjai, *J. Am. Chem. Soc.* 2012, *134*, 14208–14216.
33] R. K. Harris, E. D. Becker, S. M. C. de Menezes, R. Goodfellow, P. Granger, *Magn. Reson. Chem.* 2002, *40*, 489–505.
34] K. Akatsuka, G. Takanashi, Y. Ebina, M.-a. Haga, T. Sasaki, *J. Phys. Chem. C* 2012, *116*, 12426–12433.
35] G. J. Rees, S. T. Orr, L. O. Barrett, J. M. Fisher, J. Houghton, G. H. Spikes, B. R. Theobald, D. Thompsett, M. E. Smith, J. V. Hanna, *Phys. Chem. Chem. Phys.* 2013, *15*, 17195–17207.
36] M. Descostes, F. Mercier, N. Thromat, C. Beaucaire, M. Gautier-Soyer, *Appl. Surf. Sci.* 2000, *165*, 288–302.